Extreme Mechanics Letters 62 (2023) 102036

Contents lists available at ScienceDirect

Extreme Mechanics Letters

journal homepage: www.elsevier.com/locate/eml

Phononic crystal bandgap optimization based on a multistage grid-pixel refinement method

Chen Sun [a], Liang Wang [a], Heng Jiang [b,c], Qian Ding [a], Zhanli Liu [d,*], Yongtao Sun [a,**], Xinghao Wang [d]

[a] Department of Mechanics and Tianjin Key Laboratory of Nonlinear Dynamics and Control, Tianjin University, Tianjin, 300350, China
[b] Institute of Mechanics, Chinese Academy of Sciences, Beijing 100190, China
[c] University of Chinese Academy of Sciences, Beijing, 100049, China
[d] School of Aerospace Engineering, Tsinghua University, Beijing, 100084, China

ARTICLE INFO

Article history:
Received 16 March 2023
Received in revised form 27 April 2023
Accepted 28 May 2023
Available online 2 June 2023

Keywords:
Multistage grid-pixel refinement method
Phononic crystal bandgap optimization
Plane wave expansion method
Topology optimization

ABSTRACT

Phononic crystal (PnC) is a kind of periodic distribution structure with elastic constants and densities, which prevents the propagation of waves in the bandgap by the interaction of internal microstructures. A slow convergence process and topological ill-conditioned structure cannot fail to have noticed during the fine grid optimization process of PnC. In this paper, a multistage grid-pixel refinement method (MGPRM) is proposed to quickly obtain the high-quality PnC topology based on the fast plane wave expansion method. Combined with the MGPRM and genetic algorithm, the bandgap of PnC is used to optimize. Results show that the MGPRM combined with the optimization algorithm can provide high-quality original configurations for the tunable parameterized microstructures. Compared with invariant grids of different densities and traditional refinement methods, the MGPRM has higher quality and a faster convergence rate for the process of optimization. Using the MGPRM for multi-objective optimization, the highly nonlinear correspondence between the characteristic bandgap and the topological morphology is obtained. In addition, the dynamic response of the finite PnC microstructure plate composed of the optimized topology and the calculated transmission spectrum are in perfect agreement with the bandgap of PnC. The MGPRM is further applied to the structure design and performance optimization of PnC.

1. Introduction

Phononic crystal (PnC) is a kind of artificially periodic material or structural material that may have bandgaps, which make the wave within bandgaps decay rapidly and prevent wave propagation. Based on the characteristics of bandgaps, PnC can control acoustic and elastic waves and has broad application prospects, such as vibration isolation [1], environmental noise control [2], and directional wave propagation [3].

Analyzing the band structure of PnC plays an important role in quantitatively studying PnC performance. At present, there are many methods to calculate the band structure of PnC, among which the mainstream methods include transfer matrix method [4], finite element method [5], finite difference time domain method [6], and plane wave expansion method [7]. Among them, the plane wave expansion method (PWEM) is one of the most commonly used methods to calculate the band structure. However, the traditional PWEM can only study PnC with regular scatterers (square, round). Later, the fast plane wave expansion method (FPWEM) improves the shortcomings of the traditional PWEM and can calculate the band structure of PnC with arbitrarily distributed pixel scatterers, which makes it more widely used. Liu et al. [8] adopted the FPWEM to study the bandgap of two-dimensional (2D) steel-epoxy resin PnC in in-plane mode, out-of-plane mode and mixed mode, and the results showed that the FPWEM can effectively calculate the band structure of PnC in the three modes. Xie et al. [9] investigated the time consumed by various methods to calculate the band structure of PnC, and the results showed that the FPWEM was faster in bandgap research than the finite element method. Later in 2020, Han et al. [10] further extended the FPWEM to 2D three-phase PnC and studied the influence of volume fraction and symmetry on the bandgap.

Since the bandgap is the most significant feature of PnC and the primary indicator affecting its performance, the optimization of the bandgap has attracted widespread attention. Yi et al. [11] comprehensively summarized the recent work on the topological optimization design of PnC and proposed future directions and

* Corresponding author.
** Corresponding author.
E-mail addresses: liuzhanli@tsinghua.edu.cn (Z. Liu), ytsun@tju.edu.cn (Y. Sun).

https://doi.org/10.1016/j.eml.2023.102036
2352-4316/

challenges. Topology optimization methods of PnC have been divided into gradient [12,13] optimization methods and non-gradient optimization methods [14,15] according to whether gradient information is needed in the optimization process. Among them, the non-gradient algorithm has been widely used in many fields because its optimization results show that it is not affected by the initial configuration and has the potential to perform global searches. In the field of metamaterials, genetic algorithms have been widely used due to their strong versatility and achieved excellent results [16]. For PnC, Dong et al. [17] used the finite element method and genetic algorithm to optimize the bandgap of the symmetrical 2D solid/solid PnC under constrained and unconstrained conditions, respectively. Later, Dong et al. [18] optimized the relative bandgap of 2D asymmetric PnC based on the multi-elite genetic algorithm. These results suggest that genetic algorithms are both feasible and efficient to optimize PnC.

The work mentioned above, however, is related to single-objective optimization, whereas PnC is frequently required to have a range of features in engineering applications, including wide bandgap [19], multi-bandgap [20], lightweight [21,22], etc. A single-objective optimization algorithm cannot simultaneously satisfy the design criteria of many objectives, so it is necessary to introduce multi-objective topology optimization in PnC. The multi-objective optimization algorithm can obtain the optimal solutions by making each objective as optimal as possible under the contradictory optimization objectives. These optimal solutions give engineers more options to solve practical application problems better. The multi-objective topology optimization has been successfully applied to PnC optimization, and a large number of excellent results have been achieved. Hussein et al. [19] combined the transfer matrix method and multi-objective genetic algorithm to carry out a multi-objective optimization design of one-dimensional (1D) two-phase PnC, in which the design variables are the number of layers of material in the unit cell and the thickness of each layer. Dong et al. [20,21] performed multi-objective topological optimization based on the nondominated sorting genetic algorithm (NSGA-II) for 2D symmetric and low-symmetric porous PnC with the optimization objectives of maximizing the bandgap and minimizing the mass and analyzed the mechanism of the optimized bandgap. Hedayatrasa et al. [22] studied the topology optimization of 1D PnC plates by combining the finite element method and the multi-objective genetic algorithm and investigated the effect of different volume fractions and aspect ratios on the bandgap. Subsequently, Hedayatrasaet al. [23,24] conducted a multi-objective optimization to study porous tunable PnC plates under equibiaxial stretch and PnC plates considering in-plane equivalent stiffness. Xu et al. [25] used the FPWEM to study the optimization design of 2D three-phase PnC for in-plane wave mode, and the study showed that the multi-objective topology optimization under different multi-objective combinations had good optimization results.

In general, PnC with greater performance is more likely to be found when it is optimized in a bigger search space. Refining the grid is the most straightforward technique to expand the search space for a discrete structure segmented into pixels. However, as grid density increases, the optimization takes longer to complete and its pace of convergence slows down. In the past, some academics suggested a two-stage grid method, from coarse to fine, for optimal design to address these issues [15,17]. The multi-stage grid refinement method not only enhances the optimization efficiency but also improves the problem of the structure boundary roughness with a finer grid, which results in a smoother border for the optimized configuration. Refined grids, as compared to coarse grids, may nevertheless suffer from dispersive scatterers of the optimized topology and lower convergence rates in the later stages of optimization [25]. Adding constraints restricting the minimal size to the optimization equations [21] or eliminating the ill-conditioned structures through post-processing [26] are the two most frequently employed strategies when there is a possibility that ill-conditioned structures are included in the optimized topology. However, little work has focused on the effect of the relationship between grid density and pixel size on the optimization efficiency and Optimized results. To solve this problem, a multistage grid-pixel refinement method (MGPRM) is proposed in this paper. Unlike the grid refinement operations used in the past, the MGPRM keeps the pixel size unchanged while operating on increasing the grid density. The proposed method restrains the minimum pixel size in a simple way, reduces the dispersion of scatterers and improves the optimization efficiency under the premise of ensuring the abundant solution space.

The main content of this paper is on performing the topology optimization design of 2D two-phase PnC based on the proposed MGPRM, in conjunction with a genetic algorithm and the FPWEM. In the optimization process, the grid density of the MGPRM is changed from coarse to fine, and the performance of PnC is optimized in three stages. In Section 2, the FPWEM for calculating the band structure of PnC and the multi-objective optimization method of PnC are introduced, and the proposed MGPRM and the optimization process of this paper are described in detail. In Section 3, numerical calculations are performed and the results are analyzed. Briefly, the similarities and differences between the MGPRM, the invariant grid method and the traditional refinement grid method are discussed, and then the multi-objective optimization is performed according to different objectives. Finally, the conclusions of this article are summarized in Section 4.

2. Model and methodology

2.1. Elastic wave equation

The equation for the propagation of elastic waves in a non-homogeneous medium is expressed as

$$\rho\ddot{\boldsymbol{u}} + \nabla\left[\left[\lambda + 2\mu\right](\nabla\cdot\boldsymbol{u})\right] - \nabla\times\left[\mu\nabla\times\boldsymbol{u}\right] = \boldsymbol{0} \tag{1}$$

where ρ is the density of the material, λ and μ are the first and second parameters of the Lamé constant, $\boldsymbol{u}$ is the displacement vector, $\nabla\cdot\boldsymbol{u}$ is the divergence of the displacement vector, $\nabla\times\boldsymbol{u}$ is the curl of the displacement vector.

Since the 2D PnC is studied in this paper, Eq. (1) is decomposed into out-of-plane and in-plane modes, which are expressed as

$$\rho(\boldsymbol{r})\frac{\partial^2 u_z}{\partial t^2} = \frac{\partial}{\partial x}\left[\mu(\boldsymbol{r})\left(\frac{\partial u_z}{\partial x}\right)\right] + \frac{\partial}{\partial y}\left[\mu(\boldsymbol{r})\left(\frac{\partial u_z}{\partial y}\right)\right] \tag{2}$$

$$\begin{aligned}
\rho(\boldsymbol{r})\frac{\partial^2 u_x}{\partial t^2} = {} & \frac{\partial}{\partial x}\left[\lambda(\boldsymbol{r})\left(\frac{\partial u_x}{\partial x} + \frac{\partial u_y}{\partial y}\right)\right] + \\
& \frac{\partial}{\partial x}\left[\mu(\boldsymbol{r})\left(\frac{\partial u_x}{\partial x} + \frac{\partial u_x}{\partial x}\right)\right] + \\
& \frac{\partial}{\partial y}\left[\mu(\boldsymbol{r})\left(\frac{\partial u_x}{\partial y} + \frac{\partial u_y}{\partial x}\right)\right] \\
\rho(\boldsymbol{r})\frac{\partial^2 u_y}{\partial t^2} = {} & \frac{\partial}{\partial y}\left[\lambda(\boldsymbol{r})\left(\frac{\partial u_x}{\partial x} + \frac{\partial u_y}{\partial y}\right)\right] + \\
& \frac{\partial}{\partial x}\left[\mu(\boldsymbol{r})\left(\frac{\partial u_y}{\partial x} + \frac{\partial u_x}{\partial y}\right)\right] + \\
& \frac{\partial}{\partial y}\left[\mu(\boldsymbol{r})\left(\frac{\partial u_y}{\partial y} + \frac{\partial u_y}{\partial y}\right)\right]
\end{aligned} \tag{3}$$

where $\boldsymbol{r} = \{x, y\}$ is a spatial location vector, $\{u_x, u_y, u_z\}$ are the components of the displacement vector along the x, y and z axes, respectively. Since PnC is periodically compounded with unit cells, the material parameters $\rho(\boldsymbol{r})$, $\lambda(\boldsymbol{r})$ and $\mu(\boldsymbol{r})$ are periodic functions of the spatial position vector $\boldsymbol{r}$.

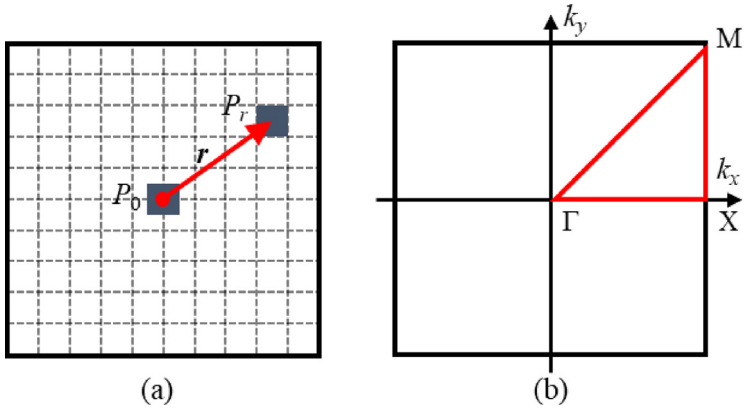

Fig. 1. (a) Square PnC with pixel P_0 in the center and arbitrary scatterer pixel P_r. $\boldsymbol{r}$ denotes the displacement vector between two pixels. (b) Reciprocal lattice of PnC, the red solid line represents the irreducible brillouin zone.

2.2. FPWEM

In 2D PnC, material parameters of unit cells can be expanded by Fourier series according to the characteristics that the material parameters are periodic functions of space. In particular, it is noted that in this section, the spatial location vector $\boldsymbol{r}$ represents the vector from the center of the unit cell to the center of the pixel as shown in Fig. 1(a). Then for the convenience of description, the material parameters are uniformly denoted by g_{m}. It can be expressed as

$$g_{\mathrm{m}}(\boldsymbol{r}) = \sum_{\boldsymbol{G}} g(\boldsymbol{G}) \cdot e^{i\boldsymbol{G}\cdot\boldsymbol{r}} \tag{4}$$

where $g(\boldsymbol{G})$ is the Fourier expansion coefficient and $\boldsymbol{G}$ is the vector of reciprocal lattice, and for 2D PnC, the $\boldsymbol{G}$ is defined as

$$\boldsymbol{G} = n_x\boldsymbol{b}_1 + n_y\boldsymbol{b}_2 \tag{5}$$

where n_x, n_y are integers and $\boldsymbol{b}_1$, $\boldsymbol{b}_2$ are the basis vectors of reciprocal lattice. For a square lattice with lattice constant a, $\boldsymbol{b}_1 = 2\pi(1,0)/a$, $\boldsymbol{b}_2 = 2\pi(0,1)/a$.

The Fourier expansion coefficient $g(\boldsymbol{G})$ can be obtained by the following equation:

$$g(\boldsymbol{G}) = \frac{1}{S}\iint_S g_{\mathrm{m}}(\boldsymbol{r}) \cdot e^{-i\boldsymbol{G}\cdot\boldsymbol{r}} d^2\boldsymbol{r} \tag{6}$$

where S is the area of the unit cell.

For PnC with a scatterer pixel P_0 at the center of the unit cell [8], the Fourier expansion coefficient $g_0(\boldsymbol{G})$ is written as

$$g_0(\boldsymbol{G}) = \begin{cases} g_{\mathrm{B}} + f\cdot(g_{\mathrm{A}} - g_{\mathrm{B}}) & ,\boldsymbol{G} = 0 \\ (g_{\mathrm{A}} - g_{\mathrm{B}})\cdot P(\boldsymbol{G}) & ,\boldsymbol{G} \neq 0 \end{cases} \tag{7}$$

where g_{A} and g_{B} represent the material parameters of scatterers and matrices respectively. $f = 1/N^2$ is the proportion of a pixel in a cell, where N is the number of unit cell edges to be divided. Since the central pixel is a square [9], the structure function $P(\boldsymbol{G})$ is written as

$$P(\boldsymbol{G}) = \begin{cases} f\,\mathrm{sinc}(\dfrac{\boldsymbol{G}_y a}{2N}), & \boldsymbol{G}_x = 0, \boldsymbol{G}_y \neq 0 \\ f\,\mathrm{sinc}(\dfrac{\boldsymbol{G}_x a}{2N}), & \boldsymbol{G}_y = 0, \boldsymbol{G}_x \neq 0 \\ f\,\mathrm{sinc}(\dfrac{\boldsymbol{G}_x a}{2N})\mathrm{sinc}(\dfrac{\boldsymbol{G}_y a}{2N}), & \boldsymbol{G}_x\boldsymbol{G}_y \neq 0 \end{cases} \tag{8}$$

where $\boldsymbol{G}_x$ and $\boldsymbol{G}_y$ are the components of the vector of reciprocal lattice $\boldsymbol{G}$ in the direction of the base vectors $\boldsymbol{b}_1$ and $\boldsymbol{b}_2$, respectively.

The relative positions of the arbitrary scatterer pixel P_r and the central scatterer pixel P_0 are shown in Fig. 1(a). According to the shift properties [10], the material Fourier expansion coefficient $g_r(\boldsymbol{G})$ for any scatterer pixel P_r can be obtained by the Fourier transformation of $g_0(\boldsymbol{G})$ and is expressed as

$$g_r(\boldsymbol{G}) = g_0(\boldsymbol{G}) \cdot e^{i\boldsymbol{G}\cdot\boldsymbol{r}} \tag{9}$$

Let $\boldsymbol{P}_{\mathrm{s}}$ be the set of all N_{s} scatterer pixels, and any scatterer pixel P_r belongs to $\boldsymbol{P}_{\mathrm{s}}$, i.e., $P_r \in \boldsymbol{P}_{\mathrm{s}}$. The Fourier coefficient of the entire metamaterial parameters [9] is written as

$$g(\boldsymbol{G}) = \sum_{P_r\in\boldsymbol{P}_{\mathrm{s}}} g_r(\boldsymbol{G}) = \sum_r g_r(\boldsymbol{G})\,\delta(\boldsymbol{r}) = g_0(\boldsymbol{G})\sum_r e^{i\boldsymbol{G}\cdot\boldsymbol{r}}\delta(\boldsymbol{r}) \tag{10}$$

where $\delta(\boldsymbol{r})$ represents the distribution of scatterers in the unit cell and is expressed as

$$\delta(\boldsymbol{r}) = \left[\delta(r_1), \delta(r_2), \ldots, \delta(r_k), \ldots, \delta\left(r_{N^2}\right)\right] = \begin{cases} 1, & P_r \in \boldsymbol{P}_{\mathrm{s}} \\ 0, & \text{other} \end{cases} \tag{11}$$

where r_k is the vector from the center of the unit cell to the center of the kth pixel. Due to the periodicity of the structure, the displacement field $\boldsymbol{u}$ is written according to Bloch's theorem as

$$\boldsymbol{u}(\boldsymbol{r}, t) = e^{i(\boldsymbol{k}\cdot\boldsymbol{r}-\omega t)}\boldsymbol{U}_{\boldsymbol{k}}(\boldsymbol{r}) \tag{12}$$

where $\boldsymbol{k}$ is the wave vector. Since $\boldsymbol{U}_{\boldsymbol{k}}(\boldsymbol{r})$ is a function with the same period as material parameters, it can be expanded into a Fourier series and is written as

$$\boldsymbol{U}_{\boldsymbol{k}}(\boldsymbol{r}) = \sum_{\boldsymbol{G}'} e^{i\boldsymbol{G}'\cdot\boldsymbol{r}}\boldsymbol{u}_{\boldsymbol{k}}(\boldsymbol{G}') \tag{13}$$

By combining Eqs. (12) and (13), it is expressed as

$$\boldsymbol{u}(\boldsymbol{r}, t) = e^{i(\boldsymbol{k}\cdot\boldsymbol{r}-\omega t)}\sum_{\boldsymbol{G}'} e^{i\boldsymbol{G}'\cdot\boldsymbol{r}}\boldsymbol{u}_{\boldsymbol{k}}(\boldsymbol{G}') \tag{14}$$

Substituting Eqs. (10) and (14) into Eq. (2), the eigen equation of the out-of-plane mode can be obtained

$$\begin{aligned} \omega^2\sum_{\boldsymbol{G}'}\rho(\boldsymbol{G}''-\boldsymbol{G}')u^z_{\boldsymbol{k}+\boldsymbol{G}}(\boldsymbol{G}') = &\sum_{\boldsymbol{G}'}\mu(\boldsymbol{G}''-\boldsymbol{G}')(k+\boldsymbol{G}')_x \\ &\times(k+\boldsymbol{G}'')_x u^z_{\boldsymbol{k}}(\boldsymbol{G}') + \\ &\sum_{\boldsymbol{G}'}\mu(\boldsymbol{G}''-\boldsymbol{G}')(k+\boldsymbol{G}')_y(k+\boldsymbol{G}'')_y \\ &\times u^z_{\boldsymbol{k}}(\boldsymbol{G}') \end{aligned} \tag{15}$$

Similarly, substituting Eqs. (10) and (14) into Eq. (3), the eigen equation of the in-plane mode can be obtained

$$\begin{aligned}\omega^2 \sum_{\boldsymbol{G}'} \rho(\boldsymbol{G}''-\boldsymbol{G}')u^x_{\boldsymbol{k}+\boldsymbol{G}} = &\sum_{\boldsymbol{G}'}[\lambda(\boldsymbol{G}''-\boldsymbol{G}')(\boldsymbol{k}+\boldsymbol{G}')_x(\boldsymbol{k}+\boldsymbol{G}'')_x+\\ &\mu(\boldsymbol{G}''-\boldsymbol{G}')((\boldsymbol{k}+\boldsymbol{G}')_y(\boldsymbol{k}+\boldsymbol{G}'')_y+\\ &2(\boldsymbol{k}+\boldsymbol{G}')_x(\boldsymbol{k}+\boldsymbol{G}'')_x)]u^x_{\boldsymbol{k}+\boldsymbol{G}}+\\ &\sum_{\boldsymbol{G}'}[\lambda(\boldsymbol{G}''-\boldsymbol{G}')(\boldsymbol{k}+\boldsymbol{G}')_y(\boldsymbol{k}+\boldsymbol{G}'')_x+\\ &\mu(\boldsymbol{G}''-\boldsymbol{G}')(\boldsymbol{k}+\boldsymbol{G}')_x(\boldsymbol{k}+\boldsymbol{G}'')_y]u^y_{\boldsymbol{k}+\boldsymbol{G}}\end{aligned} \tag{16}$$

$$\begin{aligned}\omega^2 \sum_{\boldsymbol{G}'} \rho(\boldsymbol{G}''-\boldsymbol{G}')u^y_{\boldsymbol{k}+\boldsymbol{G}} = &\sum_{\boldsymbol{G}'}[\lambda(\boldsymbol{G}''-\boldsymbol{G}')(\boldsymbol{k}+\boldsymbol{G}')_y(\boldsymbol{k}+\boldsymbol{G}'')_y+\\ &\mu(\boldsymbol{G}''-\boldsymbol{G}')((\boldsymbol{k}+\boldsymbol{G}')_x(\boldsymbol{k}+\boldsymbol{G}'')_x+\\ &2(\boldsymbol{k}+\boldsymbol{G}')_y(\boldsymbol{k}+\boldsymbol{G}'')_y)]u^y_{\boldsymbol{k}+\boldsymbol{G}}+\\ &\sum_{\boldsymbol{G}'}[\lambda(\boldsymbol{G}''-\boldsymbol{G}')(\boldsymbol{k}+\boldsymbol{G}')_x(\boldsymbol{k}+\boldsymbol{G}'')_y+\\ &\mu(\boldsymbol{G}''-\boldsymbol{G}')(\boldsymbol{k}+\boldsymbol{G}')_y(\boldsymbol{k}+\boldsymbol{G}'')_x]u^x_{\boldsymbol{k}+\boldsymbol{G}}\end{aligned} \tag{17}$$

where $\boldsymbol{G}'$ and $\boldsymbol{G}''$ is taken over the reciprocal space. However, in practice, a finite number of vectors of reciprocal lattice near the origin of the reciprocal space is usually used instead of the entire reciprocal space to find the numerical solution of the eigenvalue problem. The convergence of the PWEM is related to the number of plane waves, the larger the number of waves the better the convergence, but this also increases the computational burden. Due to the symmetry of PnC, the band structure can be obtained as long as the wave vector $\boldsymbol{k}$ sweeps the irreducible Brillouin zone, i.e., the paths $\Gamma-\mathrm{X}-\mathrm{M}-\Gamma$, as shown in Fig. 1(b).

2.3. Multi-objective genetic algorithm for PnC

The unit cell of PnC with 1/8 symmetry is shown in Fig. 2(a). The complete unit cell is obtained by transforming the blue region symmetrically three times. The unit cell of PnC is divided into $N \times N$ pixels. Due to symmetry, only the material distribution of 1/8 unit cells is taken into account. The values 0 and 1 respectively represent pixels as matrices and scatterers, as shown in Fig. 2(b). Since the material is represented by 0 or 1, the material distribution of the 2D PnC can be simply expressed as $\boldsymbol{X} = [x_1, x_2, \ldots, x_k, \ldots, x_L]$ by binary coding, where $L = (N/2)^2/2 + N/4$ represents the gene length of the unit cell.

The genetic algorithm is a global optimization method that uses information from past populations to iteratively optimize each set of populations (candidate solutions). Note that genetic algorithms are particularly suitable for multivariate nonlinear problems. The general mathematical model for multi-objective optimization is shown as

$$\begin{aligned}&\text{Find}: \boldsymbol{X} = [x_1, x_2, \ldots, x_k, \ldots, x_L]\\ &\text{Minmize}: F_1(\boldsymbol{X}),\quad F_2(\boldsymbol{X})\\ &\text{Subject to}: x_i = \begin{cases}0 & \text{, matrix}\\ 1 & \text{, scatterer}\end{cases}\end{aligned} \tag{18}$$

where F_1 and F_2 are the objective functions of the optimization. NSGA-II is used as the optimization method to enhance the properties of PnC, and more details can be found in Deb et al. [27]. The optimization process is described in Section 2.5.

2.4. MGPRM

The proposed MGPRM is obtained after improving the traditional grid refinement method (TGRM). Therefore, it is essential to initially present the TGRM. In TGRM, coarse pixels are divided into multiple finer pixels, and these fine pixels all have the same material properties as the coarse pixels, as shown in Fig. 2(c). It should be pointed out that the grid refinement rate is a two-fold refinement. The proposed MGPRM is divided into two executive parts, which are different from traditional methods. Part 1 is performed prior to the genetic operations, which aims to refine the grid and extract unit cell genes. In the process of refined scatterers, the fine pixels in the lower left corner are marked with the same material properties as the coarse pixels (marked in red), and the remaining pixels are marked with the same material properties as the matrix (marked in yellow), as shown in Fig. 2(d). Next, the results obtained from Part 1 are binary encoded as a gene of the unit cell for genetic operations. In Part 2, after completing the genetic operations and before the calculation of fitness value, each fine scatterer pixel is taken as the lower left corner of the coarse pixel for pixel coarsening. It is equivalent to a reverse process, i.e., from Fig. 2(d) to (b). The special cases of coarsening operations includes two cases, i.e., overlap and out of bounds. For case 1, there are three hinged fine scatterer pixels (red 1) at the lower position in Fig. 2(e). Three matrix pixels next to each scatterer pixel are converted to scatterer pixels and given the yellow 1 designation after Part 2 of the MGPRM has been completed. The regions of overlap is presented in the three coarse scatterer pixels and are identified by dark shading. To solve this problem, the union of these pixels is taken. The boundary of the scatterer block taken by the union of three coarse pixels is shown as the green line. For case 2, since the design space is restricted to the 1/8 single cell region, the fine pixels close to the edge may have a part beyond the restricted region after performing Part 2 of the MGPRM. The fine scatterer pixels (red 1) close to the boundary exceed the boundary after performing Part 2 of the MGPRM in Fig. 2(e). In this case, the coarse pixels are cropped and left within the 1/8 single cell region. The blue line (in Fig. 2(e)) is the boundary of the scatter block after the coarse pixel interception.

Compared to the TGRM, the MGPRM can effectively alleviate topological discontinuities and increase the size of discrete pixels, indicating that it improves the quality of configurations. If the matrix (yellow 0) framed by the blue square is changed to the scatterer (red 1) in Fig. 2(d), the shape of the scatterer block is unchanged after the implementation of Part 2. Thus, the MGPRM can reduce the structural topology space of the solution.

2.5. Optimization process

The whole optimization process (in Fig. 3) is described as follows:

Step 1: Initialize parameters, such as lattice constants of PnC, population size, the maximum number of iterations, etc. The randomly generated population is used as the parent population $\boldsymbol{P}_{\mathrm{P}}$. Then the iteration calculator t and key generation t_{key} are both initialized, and t_{key} is set as the executed criterion for the MGPRM.

Step 2: Perform genetic algorithm operations: selection, crossover, and mutation. The binary tournament selection method is used for the selection operation, and the average method is used for the crossover operation and mutation operation. The newly created population is referred to as the offspring population $\boldsymbol{P}_{\mathrm{O}}$.

Step 3: Before calculating the objective functions F_1 and F_2, check whether the iteration calculator t is greater than or equal to the key generation t_{key}. If the iteration calculator reaches the key generation, calculate the fitness after executing Part 2 of the

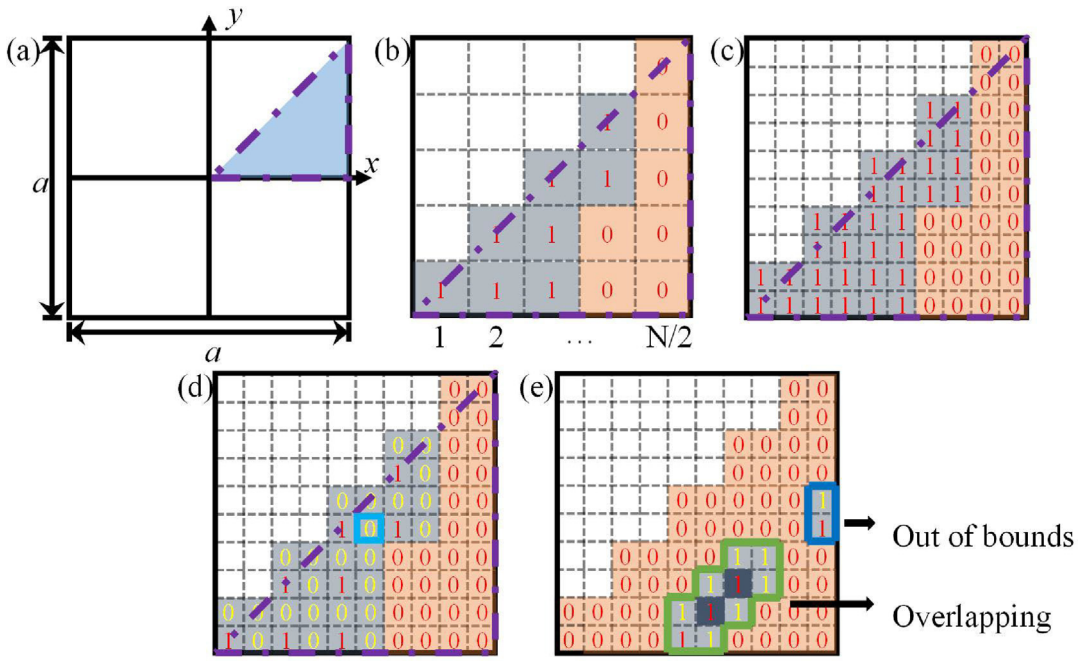

Fig. 2. Dispersion and grid refinement of unit cell. (a) The unit cell with 1/8 symmetry. (b) 1/8 zone of separated unit cell. (c) Traditional refinement grid method. (d) Proposed refinement method. (e) Coarse pixel combination and cropping method. . (For interpretation of the references to color in this figure legend, the reader is referred to the web version of this article.)

refined grid; otherwise, calculate the fitness directly. Note that the FPWEM is used to calculate the band structure of PnC.

Step 4: Merge the parent population and offspring population: $\boldsymbol{P}_{\mathrm{A}} = \boldsymbol{P}_{\mathrm{P}} \cup \boldsymbol{P}_{\mathrm{O}}$, and then conduct non-dominant sorting and crowding distance calculation operations for the merged population $\boldsymbol{P}_{\mathrm{A}}$.

Step 5: A new population is selected based on the ranking and crowding and the population is used as the new parent population, and the iteration calculator is increased by one: $t = t + 1$.

Step 6: Check if the maximum number of iterations is reached. Exit the loop when the maximum number of iterations is reached, otherwise continue to the next step.

Step 7: Check whether the condition of the MGPRM is met. If so, perform Part 1 of the MGPRM and skip back to Step 2; otherwise, skip back to Step 2 directly.

For multistage, multiple key generations need to be set. In addition to this setting, other methods can be used, such as executing the MGPRM if the optimal solution remains unchanged in the population for 10 consecutive generations.

3. Numerical results and discussion

Lead and epoxy resin are selected as the scatterer and matrix of PnC, respectively. The specific material parameters are listed in Table 1. The lattice constant of PnC with 1/8 symmetry is $a = 0.02$ m. According to the formula $c_{\mathrm{t}} = \sqrt{\mu/\rho}$, the transverse wave velocity of the matrix is $c_{\mathrm{t}} = 1160.8$ m/s. The normalized frequency $\Omega = \omega a/(2\pi c_{\mathrm{t}})$ is selected to characterize the frequency information, which can eliminate the influence of size and material on the results and make the proposed optimization method more general.

3.1. Verify the validity of the proposed MGPRM

To demonstrate the performance of the MGPRM, we perform single-objective optimization using different grid dividing methods and analyze the process and results in this section.

Table 1
Material parameters of PnC.

Material	Density ρ (kg/m^3)	Elastic modulus E (GPa)	Shear modulus μ (GPa)
Lead	11 600	40.8	14.9
Epoxy	1180	4.35	1.59

The optimization method in this section uses a genetic algorithm. Compared with the NSGA-II, the genetic algorithm does not have the process of non-dominated sorting and crowding distance calculation, so it is simpler to optimize PnC. Details of the genetic algorithm can be found in Han et al. [28]. This section carries out the optimization design with the objective function of maximizing the single relative bandgap width (RBW), and its mathematical model is expressed as

$$\begin{aligned} &\text{Find}: \boldsymbol{X} = [x_1, x_2, \ldots, x_k, \ldots, x_L] \\ &\text{Maxmize}: F(\boldsymbol{X}) = \frac{\Delta\omega_n}{\omega_n^c} = 2\frac{\min\omega_{n+1}(\boldsymbol{k}) - \max\omega_n(\boldsymbol{k})}{\min\omega_{n+1}(\boldsymbol{k}) + \max\omega_n(\boldsymbol{k})} \\ &\text{Subject to}: x_i = \begin{cases} 0 & \text{, epoxy} \\ 1 & \text{, lead} \end{cases} \end{aligned} \tag{19}$$

where $\omega_n(\boldsymbol{k})$ is the frequency at the wave vector $\boldsymbol{k}$ of the nth band. The objective function F denotes the RBW between the nth and $n+1$th bands. Later, for the convenience of the narrative, the lower boundary index of the bandgap refers to the index of the bandgap, i.e., the nth bandgap denotes the bandgap between the nth and $n+1$th bands.

Since this section mainly focuses on comparing the differences in optimization under different grids, the objective function is chosen as the most common in the first RBW under out-of-plane modes. Previous studies [20,25] have shown that the refinement of the grid has a more pronounced effect on the bandgap at a coarser grid. However, with the continuous refinement of the grid, when the grid is fine to a certain extent, the grid density has less effect on the bandgap. In this topology optimization,

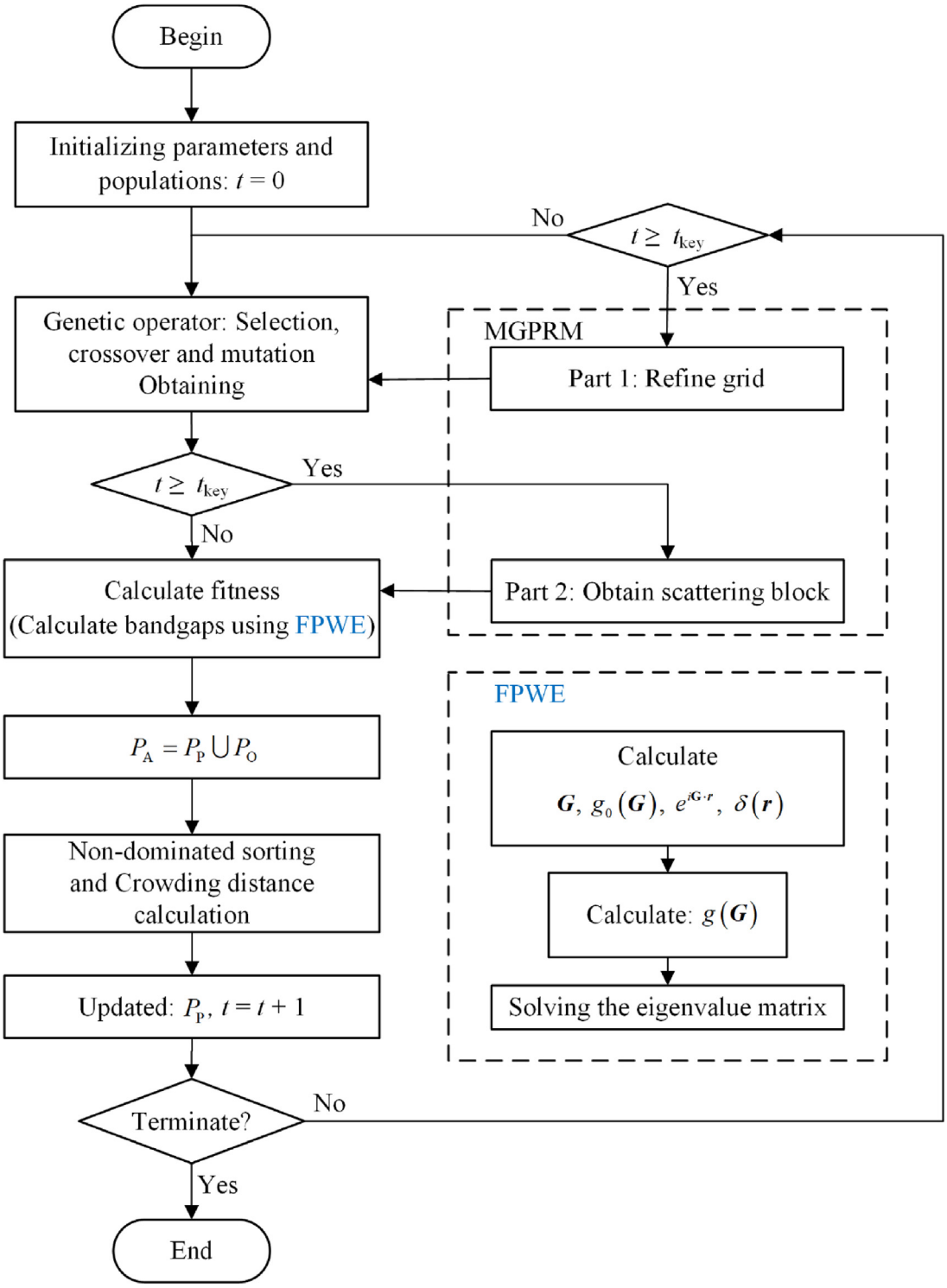

Fig. 3. Flow chart of optimization process.

considering the grid dependence problem on the bandgap effect and the computational efficiency, the unit cell is divided into three types of grids, i.e., 10×10, 20×20 and 40×40.

Both the TGRM and the proposed MGPRM are divided into three stages, and the total number of iterations is set as 100. In addition, the key generations were set to 20 and 50 generations. In other words, the number of iterations in each grid state is 20, 30 and 50 generations respectively, and the three grids change from coarse to fine in turn. At the same time, the invariable grids of 10×10, 20×20 and 40×40 are optimized respectively for reference and comparison with the variable grid method. It is pointed out that the following examples also use the key generations to set the multiple stages.

The parameters in the genetic algorithm are set as population size $P_n = 30$, crossover probability $P_c = 0.9$, and mutation probability $P_m = 0.02$. The calculated evolutionary curves and unit cell topologies are shown in Fig. 4.

As shown in Fig. 4(a), the light blue dashed line, green solid line, dark blue dotted line, black dashed line and red solid line correspond to the evolutionary curves of the 10×10 grids,

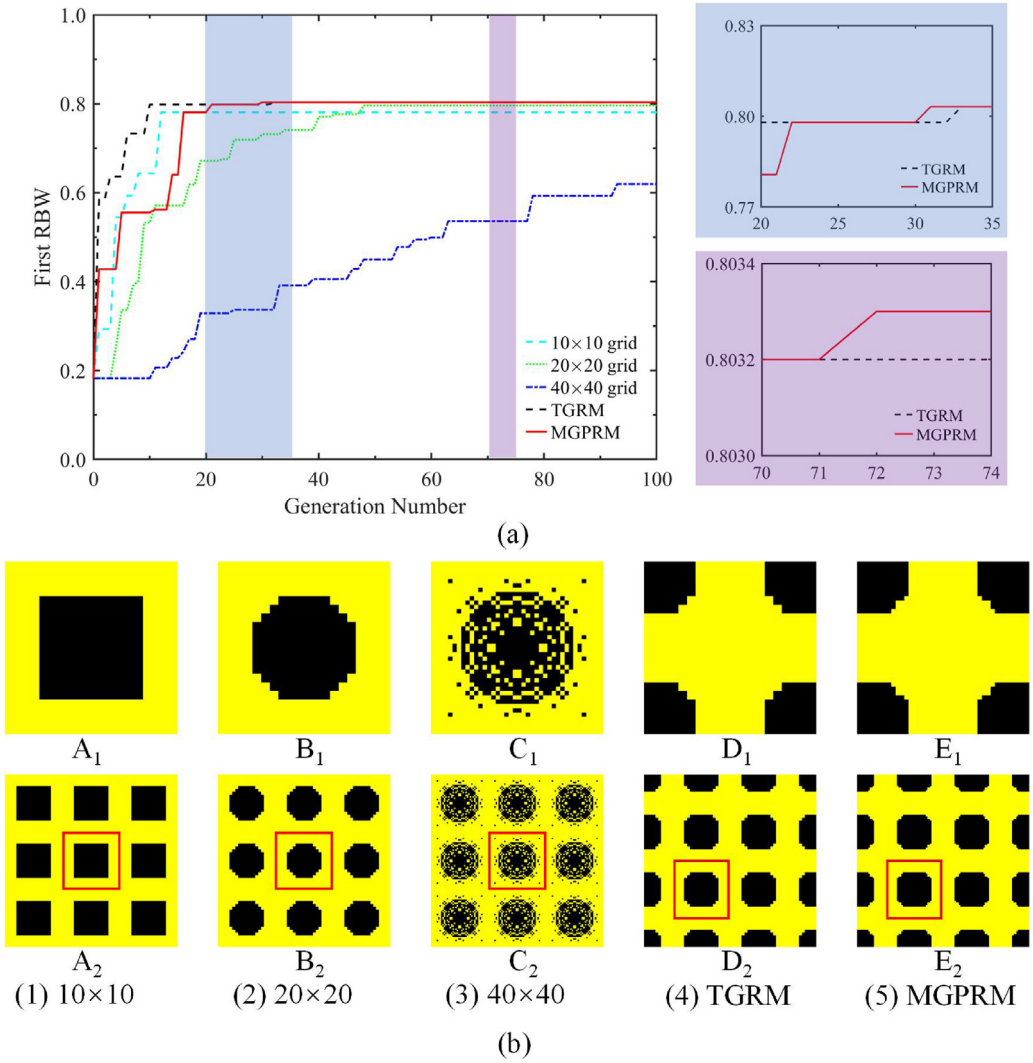

Fig. 4. Optimization of the RBW in the out-of-plane mode. (a) Evolutionary curves. (b) Optimized topologies with different grids: $A_1 - E_1$ are optimized unit cells; $A_2 - E_2$ are optimized 3 × 3 topological microstructures. . (For interpretation of the references to color in this figure legend, the reader is referred to the web version of this article.)

20 × 20 grids, 40 × 40 grids, the TGRM and the proposed MGPRM, respectively. The optimized topologies obtained by different grids or grid refinement methods after 100 generations are shown in Fig. 4(b). The corresponding bandgap boundaries and the first RBW for these optimized topologies are listed in Table 2. Among them, the maximum value (0.8033) of the first RBW is optimized by the MGPRM, and the minimum value (0.6195) of the first RBW is optimized by 40 × 40 grids. In particular, by observing the optimized unit cell topology, it can be found that there is a huge gap between the two topologies, B_1 and D_1, as shown in Fig. 4(b). The reason for this large difference is that the unit cell of PnC has period translation symmetry. Although the period translation may lead to a flip in the adjacent band modes [29], this change does not affect the band structure and therefore does not affect the bandgap width. Thus, the two structures of scatterers dispersed in the four corners and concentrated in the center of the unit cell are equivalent topologies for the analysis of the bandgap width. To better analyze the nonlinear relationship between the topological structure and the bandgap, the structure of scatterers distributed near the center is selected as the observation unit cell, and the microstructure of 3 × 3 unit cells is used to show the $A_2 - E_2$ in Fig. 4(b). Moreover, the scatterers of the optimized unit cell topology under the invariable grids are all concentrated

Table 2
Bandgap boundaries and the first RBW for optimized topology with different grids.

Grid type	Upper boundary	Lower boundary	First RBW
10 × 10	0.3087	0.7041	0.7807
20 × 20	0.3063	0.7113	0.7961
40 × 40	0.3593	0.6818	0.6195
TGRM	0.3052	0.7147	0.8032
MGPRM	0.3048	0.7140	0.8033

masses similar to circles or squares, except for the scatterers of the optimization results under the 40 × 40 grids which are more discrete. Similar phenomena have also appeared in Liu et al. [8] and Dong et al. [17].

All evolution curves are monotonically ascending, indicating that the genetic algorithm has a good effect on the RBW optimization of PnC, as shown in Fig. 4(a). In addition, except for the 40 × 40 grids, the evolution curves of other grids tend to be stable, which indicates that the optimization process has reached convergence.

Comparing the evolution curves under different invariant grids reveals that both 10 × 10 and 20 × 20 grids have a faster convergence rate than 40 × 40 grids, while having a wider

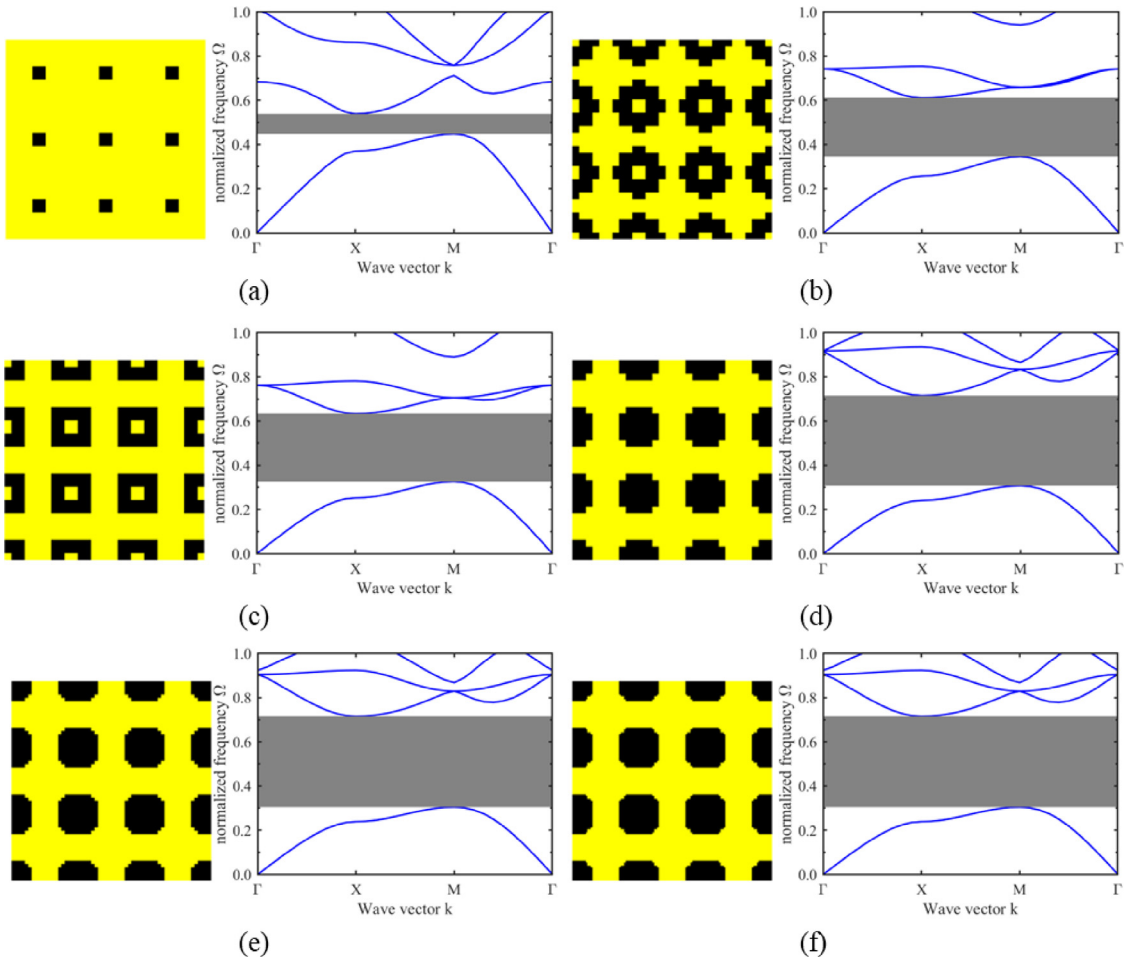

Fig. 5. 3 × 3 Microstructure and corresponding band structure of optimal individuals using MGPRM in different generations. (a) Initial generation. (b) 10th generation. (c) 15th generation. (d) 29th generation. (c) 35th generation. (d) 100th generation.

relative bandgap. The RBW of 20 × 20 grids is larger than that of 10 × 10 grids, which is consistent with the law of larger bandgap width for finer grids summarized by Dong et al. [20]. However, in the 100 generations optimization, the finer grids violate this law, which is caused by the fact that the 40 × 40 grids did not reach the convergence state. Moreover, by observing the optimized topology of 40 × 40 grids after 100 generations, there are a large number of discrete scatterers, discontinuities and other ill conditioned structures in the optimized topology. The reason for non-convergence after 100 generations of optimization under 40 × 40 grids is that more iterations are required. After the grid refinement, the solution space becomes larger and more computational solutions are needed, which makes the optimization time longer. Although Dong et al. [20] achieved a convergent result under 60 × 60 grids or even 100 × 100 grids, the convergent result is obtained after 3000 generations of optimization. The results indicate that using coarse grids at the beginning is conducive to speeding up the convergence rate and saving optimization time.

The evolution curves of the TGRM and the proposed MGPRM have faster convergence rates than traditional methods. At the same time, both of their corresponding final optimized unit cell topologies have a smoother boundary. Since genetic algorithms are heuristic algorithms with randomness, the optimization speed is uncertain and random at the beginning. Therefore, more attention should be paid to the optimization speed after the RBW is optimized to a certain value. The evolution curve using the TGRM reaches 0.7980 in the 11th generation, but it does not evolve to 0.8032 until the 33rd generation. After that, no more excellent individuals are obtained. This is because the TGRM still cannot overcome the problem of slow convergence due to large search space in the case of high grid density and is difficult to obtain a better convergence structure. Although the evolution curve of the MGPRM is 0.7808 until the 17th generation, the curve rapidly evolves twice to reach 0.8032 in the 22nd and 31st generations. As shown in Fig. 4(a), the drawing of partial enlargement in blue shading shows that the optimization speed of the MGPRM is faster than that of the TGRM when a wide RBW is reached. As shown in the drawing of partial enlargement in purple shadow in Fig. 4(a), the evolution curve of the MGPRM has evolved to 0.8033 after 72 generations. This is a slight improvement, but not easy in such a large search space. In addition, the boundary of the final optimization result of the MGPRM (topology E_1) is smoother than that of the TGRM (topology D_1) in Fig. 4(b). In addition, the new MGPRM should be no longer produce useless structures such as the dispersion of small pixels in the fine grid, so it has a smaller search space than the TGRM and often has a faster and better convergence effect. These results indicate that the MGPRM can obtain topologies with wider RBW and better structural quality than the TGRM within 100 generations.

For further analysis, the microstructures of PnC with the largest fitness values in the initial, 10th, 15th, 29th, 35th and 100th generation populations in the evolution curve using the MGPRM are respectively shown in Fig. 5, and the corresponding bandgap boundaries and RBW are listed in Table 3. Fig. 5 illustrates that PnC topology has evolved from the initial square seed

Table 3
Bandgap boundaries and the first RBW of optimal individuals using MGPRM in different generations.

Generation number	Upper boundary	Lower boundary	First RBW
0	0.4484	0.5384	0.1825
10	0.3455	0.6112	0.5555
15	0.3262	0.6333	0.6195
29	0.3074	0.7156	0.7980
35	0.3052	0.7147	0.8032
100	0.3048	0.7140	0.8033

structure to a topological configuration suitable for expanding the first RBW. Particularly, after obtaining the appropriate topological configuration as shown in Fig. 5(d), the configuration of the optimal individual does not change dramatically. The edge of the configuration becomes smoother with the gird denser, and the bandgap width also increases slightly. Note that the direction of topology change is not completely in a particular direction, especially in the early optimization, as shown in Fig. 5(b–c). For example, annular scatterers that can open a medium bandgap width appear in the early optimization, but with the further expansion of the bandgap, the holes in the middle of the annular scatterers disappear, resulting in a solid block topology. The results indicate that the genetic algorithm has excellent global search ability in PnC optimization.

3.2. Multi-objective optimization of PnC

3.2.1. Case 1, multi-objective optimization of the first relative bandgap and normalized mass in the out-of-plane mode

While expanding the width of the bandgap, it is important for practical applications to realize the lightweight of PnC. Therefore, in this section, the RBW of out-of-plane mode and mass are chosen as the optimization objectives, and the mathematical model of multi-objective optimization is shown as

$$\begin{aligned}
&\text{Find}: \boldsymbol{X} = [x_1, x_2, \ldots, x_k, \ldots, x_L] \\
&\text{Maxmize}: F_1(\mathbf{X}) = \frac{\Delta\omega_n}{\omega_n^c} = 2\frac{\min\omega_{n+1}(k) - \max\omega_n(k)}{\min\omega_{n+1}(k) + \max\omega_n(k)} \\
&\text{Minmize}: F_2(\mathbf{X}) = \frac{1}{L}\sum x_i \\
&\text{Subject to}: x_i = \begin{cases} 0 & \text{, epoxy} \\ 1 & \text{, lead} \end{cases}
\end{aligned} \tag{20}$$

where the optimization objective F_1 is the first RBW and the optimization objective F_2 is the normalized mass.

The parameters of the multi-objective genetic algorithm are set as population size P_n, crossover probability P_c and mutation probability P_m, which are the same as those of the genetic algorithm in Section 3.1.

The Pareto optimal solutions for the multi-objective optimal design with maximization of the first RBW and minimization of the unit cell mass are shown in Fig. 6(a). The horizontal and vertical axes represent the first RBW and normalized mass, respectively. The blue dots represent the non-dominated optimum solutions, while the red pentagrams represent the four selected topologies, namely A, B, C, and D. It can be seen from Fig. 6(a) that the optimal solutions are relatively evenly distributed on the Pareto optimal front, which indicates that the multi-objective optimization between the RBW and mass is effective. The normalized mass of the unit cell is found to increase with the increase of the first RBW, which means that there is a contradiction between maximizing the first RBW and minimizing the normalized mass. This means that the two objectives cannot be solved optimally at the same time. Although the positions of the individual solutions are different, all solutions are equal and mutually non-dominant with each other. If there is a higher requirement for lightweight, the selection can be made from the lower left corner of Fig. 6(a). Conversely, if the problem under study is more interested in the width of the bandgap, the selection can be made from the upper right corner of the solutions. Further, as seen in Fig. 6(a), the overall trend of the bending changes from gentle to steep. Among them, near the optimized topology C, there is a watershed of the influence of mass on the RBW. Before this point, there is a significant increase in the RBW as the normalized mass of the unit cell increases. However, after this point, a large increase in the normalized mass is required to produce a slight increase in the RBW. This law has a good guiding significance for the application of PnC considering lightweight design. Moreover, this law indicates that there is a limit to the adjustment of the single bandgap by tuning the mass. This indicates other methods to widen the bandgap, such as the use of piezoelectric materials, can be considered after reaching a point where the mass and the single bandgap are relatively balanced [30].

Table 4
Bandgap boundaries, the first RBW and normalized mass of the selected solutions in Case 1.

Topology	Bandgap boundary	First RBW	Normalized mass
A	[0.4484, 0.5384]	0.1825	0.0400
B	[0.3624, 0.6021]	0.4970	0.1075
C	[0.3218, 0.6596]	0.6885	0.1900
D	[0.3063, 0.7129]	0.7979	0.3000

The evolutionary curves for maximizing the first RBW and minimizing the normalized mass are shown in Fig. 6(b). The evolution curve of RBW shows that the individual with the largest RBW in the population always has an increasing value of the RBW, which is due to the nature of the genetic algorithm to prefer the best individuals when generating new populations. Note that the normalized mass does not monotonically decrease but suddenly increases at the 20th generation. Since the ultralight topology without a bandgap is deleted after the 20th generation population to improve the population quality, the minimum normalized mass suddenly increases. However, since configurations without bandgaps are removed in subsequent populations, this results in relatively few points in the region with the small RBW in Fig. 6(a).

From the optimal solutions in Fig. 6(a), solution D with the largest RBW and solution A with the least normalized mass were selected, and then two solutions B and C with relatively uniform objective values were selected. These selected structures and corresponding band structures are shown in Fig. 7.

Among optimized topologies A, B, C and D, and the first RBW and normalized mass corresponding to different optimized topologies are different, as shown in Fig. 7. Specific values are shown in Table 4.

The configuration of the unit cell on the Pareto optimal front changes regularly with the increase of the first RBW and the decrease of normalized mass. The scatterer starts from the initial small square, first forms a structure with four prominent corners, and then gradually transitions into a circular structure. The configuration change process indicates that the bandgap of PnC is not only related to the normalized mass of unit cells, but also to the scattering shape. Therefore, topological optimization to improve the performance of materials is very helpful. The single-objective optimization result in Fig. 5(f) is basically similar to the optimization topology obtained by multi-objective optimization in Fig. 7(d). The two optimized topologies corresponding to the RBW are 0.8033 and 0.7979 respectively, which means that single-objective optimization can obtain a topology structure with a larger RBW. Therefore, the single-objective optimization can produce superior results while pursuing the maximization of the

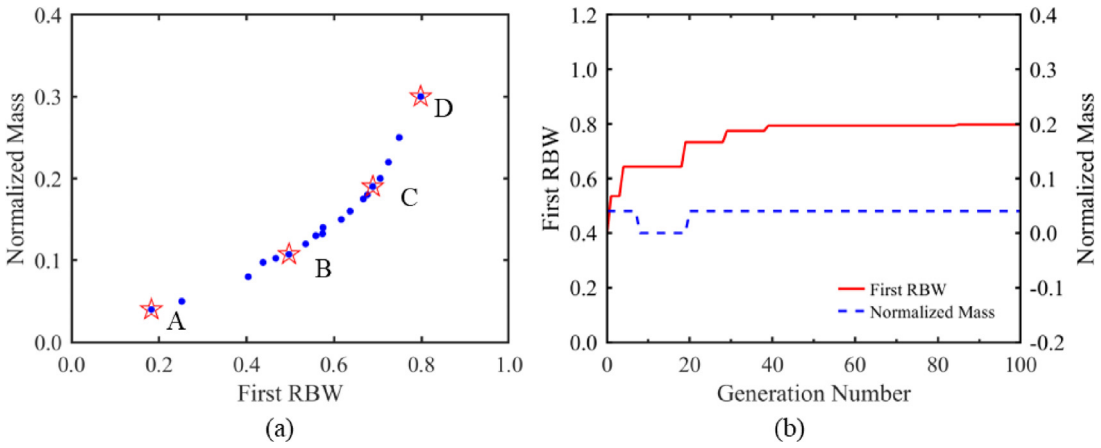

Fig. 6. Pareto optimal solutions and evolutionary curves. (a) For the optimal solutions of case 1. (b) Evolutionary curves of the first RBW and the normalized mass, the red solid and the blue dashed line represent the first RBW and the normalized mass, respectively.

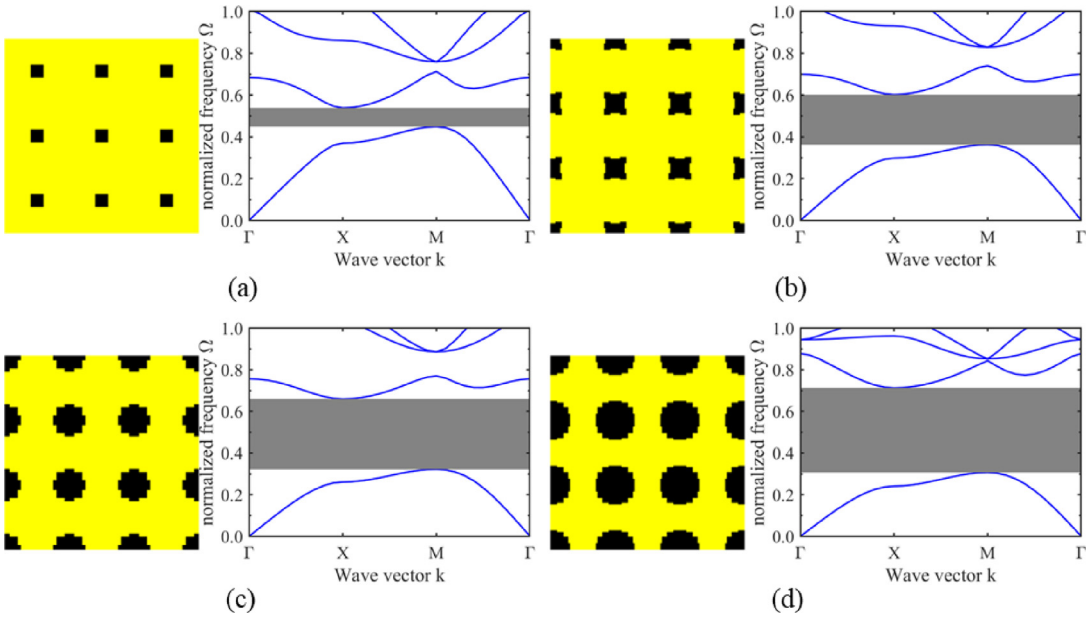

Fig. 7. The 3 × 3 microstructure and corresponding band diagram of the selected solutions. (a) Optimize topology A. (b) Optimize topology B. (c) Optimize topology C. (d) Optimize topology D.

bandgap. However, if the factor of weight needs to be considered, the multiple results provided by multi-objective optimization are also very meaningful for the lightweight of PnC.

It is worth mentioning that the normalized mass in this paper is expressed in the same way as the scatterer filling rate. Therefore, the filling rate of optimal topology D with the maximum wide bandgap in the multi-objective optimization solutions is 0.3, as shown in Fig. 7(d), which is consistent with the single-objective optimization result of Dong et al. [17].

3.2.2. Case 2, multi-objective optimization of the third and fifth RBW of in-plane modes

Realizing vibration isolation and noise reduction in multiple frequency bands is of great significance for industrial manufacturing. Therefore, we consider the optimal design of the two bandgaps of PnC in case 2. The more complex wave under in-plane mode is studied in this section. Because the in-plane coupled wave has rigid body displacement in two directions, the first two bands overlap at the point Γ. This is an inherent property of the in-plane coupled wave, so there are no bandgaps between the first two bands in the in-plane mode. After comprehensive consideration, the 3rd bandgap and the 5th bandgap are selected as the optimization objectives, and the mathematical equation of the optimization problem could be expressed as

$$\begin{aligned}
&\text{Find}: \boldsymbol{X} = [x_1, x_2, \ldots, x_k, \ldots, x_L] \\
&\text{Maxmize}: F_1(\boldsymbol{X}) = \frac{\Delta\omega_{n_1}}{\omega^c_{n_1}} = 2\frac{\min \omega_{n_1+1}(\boldsymbol{k}) - \max \omega_{n_1}(\boldsymbol{k})}{\min \omega_{n_1+1}(\boldsymbol{k}) + \max \omega_{n_1}(\boldsymbol{k})} \\
&\text{Maxmize}: F_2(\boldsymbol{X}) = \frac{\Delta\omega_{n_2}}{\omega^c_{n_2}} = 2\frac{\min \omega_{n_2+1}(\boldsymbol{k}) - \max \omega_{n_2}(\boldsymbol{k})}{\min \omega_{n_2+1}(\boldsymbol{k}) + \max \omega_{n_2}(\boldsymbol{k})} \\
&\text{Subject to}: x_i = \begin{cases} 0 & \text{, epoxy} \\ 1 & \text{, lead} \end{cases}
\end{aligned} \tag{21}$$

where F_1 is the 3rd RBW and F_2 is the 5th RBW, where $n_1 = 3$ and $n_2 = 5$. The parameters in the multi-objective genetic algorithm only change the population size $P_n = 30$ to 40, and the other parameters remain unchanged.

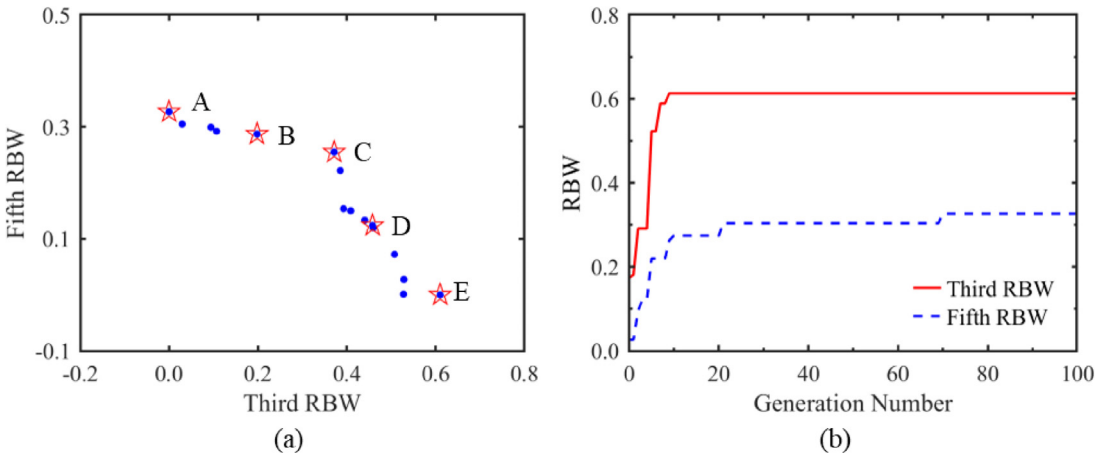

Fig. 8. Pareto optimal solutions and evolutionary curves. (a) For the optimal solution set of case 2, (b) Evolutionary curves of the 3rd RBW and 5th RBW, red straight line and blue dashed line represent the 3rd RBW and 5th RBW respectively.

Pareto optimal solutions obtained by multi-objective optimization of the 3rd and 5th RBW are shown in Fig. 8(a). The horizontal axis represents the 3rd RBW and the vertical axis represents the 5th RBW. The blue dots represent the obtained optimal solutions, while the red pentagrams represent the five selected typical structures and are labeled as A, B, C, D, and E respectively. The solutions are evenly distributed on the Pareto front, which indicates that the multi-objective optimization can obtain good results for the two bandgaps of case 2. The overall variation trend of the solutions shows that when the 3rd RBW increases, the overall trend of the 5th RBW declines, and the amplitude of decline changes greatly. The advantage of Pareto solutions is to provide a variety of mutually non-dominant choices, which can be selected according to the actual demand. For low frequencies, the corresponding structures can be chosen in the lower right corner of Pareto optimal solutions. One the contrary, the structures with high frequency bandgaps are obtained at the upper left.

Fig. 9 shows the 3 × 3 topological microstructures and the corresponding band structures of the selected typical solutions. In addition, the corresponding boundaries of the 3rd and 5th bandgaps and the corresponding RBW are shown in Table 5. Interestingly, the variation in the 3rd bandgap is primarily due to the variation in the upper boundary of the bandgap, while the change of the 5th bandgap depends on the lower boundary of the bandgap as indicated in Fig. 9.

As can be seen from Fig. 9, the optimized topologies of the unit cell change regularly. When the 5th RBW is larger, the scatterer shape in a unit cell is similar to a ring. As the 5th RBW decreases and the 3rd RBW increases, the hole in the middle of the scatterer ring shrinks until it closes. In addition, the outer profile of the scatterer changes from a similar circular shape to a final square shape. The optimized topology C is a very valuable structure, which obtains a wide relative bandgap at both the 3rd and 5th bandgap. Fig. 9 illustrates that different bandgaps correspond to different topological features, and multi-objective optimization can find such complex nonlinear relationships, which are difficult to find by traditional parameter regulation and single-objective optimization. Therefore, multi-objective optimization has a great practical role in guiding the regulation of the bandgap.

3.3. Frequency response of a finite PnC plate

The band structure described above is calculated based on the structure of the infinite periodic arrangement of unit cells. However, in practical engineering, the structures that are really applied are limited, and the smaller the limited structure, the more beneficial to the practical application. In addition, assuming that the structure is infinite, the small attenuation is amplified, which leads to an overestimation of the vibration isolation and noise reduction capability of the optimized topology. Therefore, it is necessary to introduce the frequency response function T [31] to evaluate the attenuation effect of the finite structure, and T can be expressed as

$$T = 20 \lg \frac{d_o}{d_i} \tag{22}$$

where d_o and d_i are the displacement amplitudes of the output port and the input port respectively.

The model of the 5 × 10 PnC microstructure plate is shown in Fig. 10(a), which is composed of optimized unit cell topology (Fig. 9(c)). The specified displacement is input on the left of the PnC microstructure plate, and the input displacement amplitude is $d_i = 1$ mm. The output displacement amplitude d_o is received on the right of the PnC microstructure plate, and the transmission spectrum of the model is obtained by Eq. (22), as shown in Fig. 10(b).

The red and purple lines represent the upper and lower boundaries of the 3rd and 5th bandgaps respectively, while the black curve represents the transmission curve. The transmission curve has two vibration attenuation peaks, among which the first vibration attenuation peak is −113 dB and the second vibration attenuation peak is −170 dB. The attenuation peaks of the transmission curve and the location of the bandgaps are in good agreement, which indicates that the topology designed by multi-objective optimization is still effective in the finite structure.

Fig. 10(c) shows harmonic responses of the PnC microstructure plate at the normalized frequency $\Omega = 0.4, 0.6, 0.8, 1.0$. The elastic wave of in-plane mode can pass through the finite structure model at $\Omega = 0.4$ and 0.8. However, when $\Omega = 0.6$ and 1.0,

Table 5
Bandgap boundaries, 3rd RBW and 5th RBW of the selected solutions in Case 2.

Topology	3rd bandgap	5th bandgap	3rd RBW	5th RBW
A	0	[0.8011, 1.1139]	0	0.3267
B	[0.5417, 0.6607]	[0.8197, 1.0944]	0.1979	0.2871
C	[0.5104, 0.7433]	[0.8997, 1.1624]	0.3716	0.2548
D	[0.5081, 0.8100]	[0.9657, 1.0932]	0.4581	0.1239
E	[0.5057, 0.9499]	0	0.6103	0

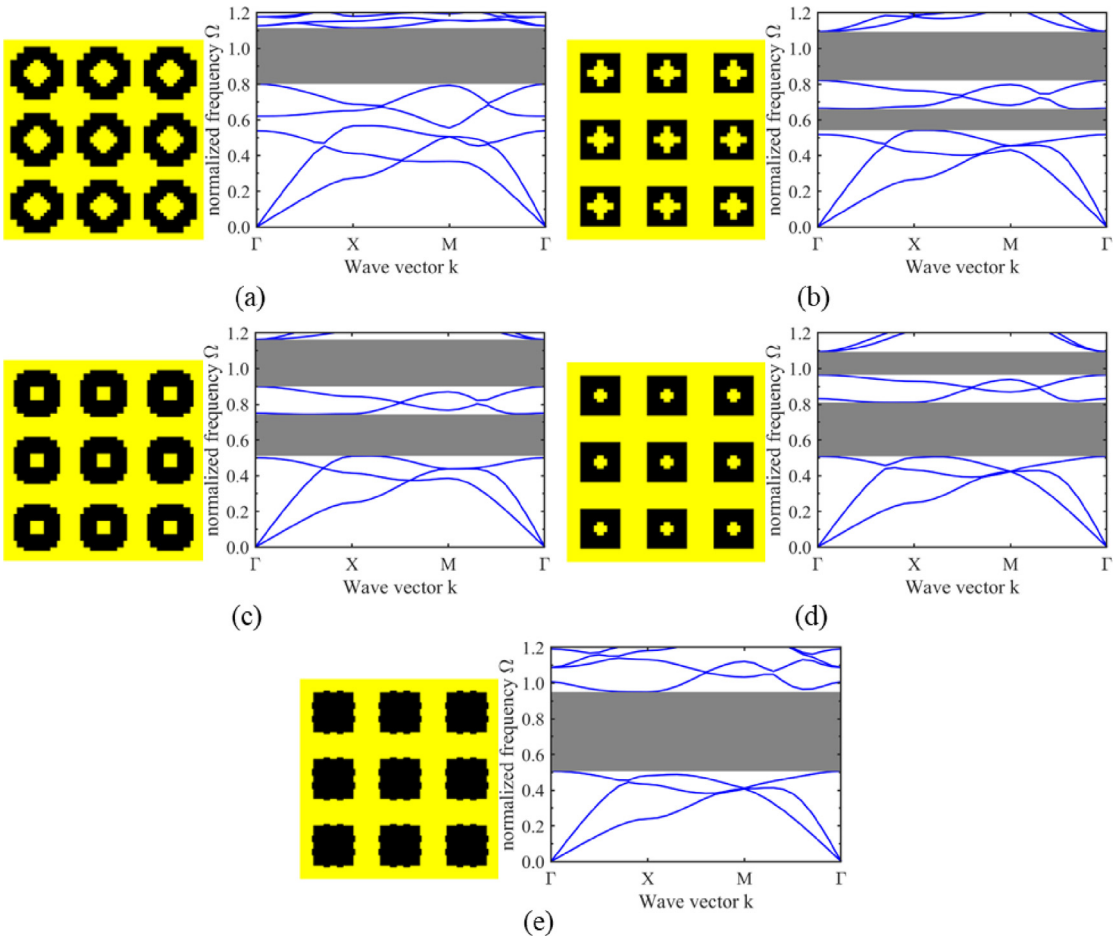

Fig. 9. The 3 × 3 microstructure and corresponding band diagram of the selected solutions. (a) Optimize topology A. (b) Optimize topology B. (c) Optimize topology C. (d) Optimize topology D. (e) Optimize topology E.

the elastic wave of in-plane mode decays rapidly and cannot pass through the finite structure model.

The phenomenon of elastic wave propagation and inhibition in the PnC microstructure plate is consistent with the results of the bandgap and the transmission spectrum. In particular, when normalized frequency $\Omega = 0.6$, the elastic wave propagates the length of two unit cells. However, when normalized frequency $\Omega = 1.0$, the elastic wave propagates the length of one unit cell. This indicates that the PnC microstructure plate has a better attenuation effect on the elastic wave when normalized frequency $\Omega = 1.0$, which is consistent with the fact that the first vibration attenuation peak is smaller than the second vibration attenuation peak in the transmission curve. Based on this phenomenon, when using the bandgap characteristics of PnC for vibration isolation and noise reduction, not only should we consider whether there is a bandgap near the target frequency, but also should consider the actual attenuation capacity of the PnC microstructure. Otherwise, the PnC microstructure plate may face the problem of insufficient attenuation performance or too strong attenuation performance.

4. Conclusion

In this paper, we propose the MGPRM and combine the FP-WEM and the genetic algorithm to optimize the bandgap of PnC. The main conclusions of are as follows:

1. For single-objective optimization, the bandgap result of the proposed MGPRM is 0.8033, which is larger than that of other grid types. This shows that the proposed MGPRM has better convergence results than other grid types and the corresponding evolution curve of MGPRM shows a fast convergence rate.
2. For multi-objective optimization, there is a structure with the 3rd RBW being 0.3716 and the 5th RBW being 0.2548 in the middle of the Pareto optimal front, which indicates that the proposed method can achieve the optimal design of the specified multi-bandgap. By further observing the topological configurations corresponding to different bandgap distributions, the multi-objective optimization has the advantage of discovering the physical nonlinear relationship between the bandgap and the PnC topology.
3. The transmission spectrum of the finite PnC microstructure plate is consistent with the bandgap of PnC, and the first and second vibration attenuation peaks are −113 dB and −170 dB, respectively. The amplitude field of the PnC microstructure plate shows the rapid attenuation of elastic waves within the bandgap, which well shows the vibration isolation characteristic of the PnC bandgap. In particular, elastic waves near the first peak frequency propagate further in the amplitude field than those near the second peak frequency, which is consistent with the propagation property in the transmission curve.

The MGPRM proposed in this paper is used in bandgap optimization design and phased optimization to improve the iteration rate. Moreover, the method can be extended to three-dimensional space for phased optimization design.

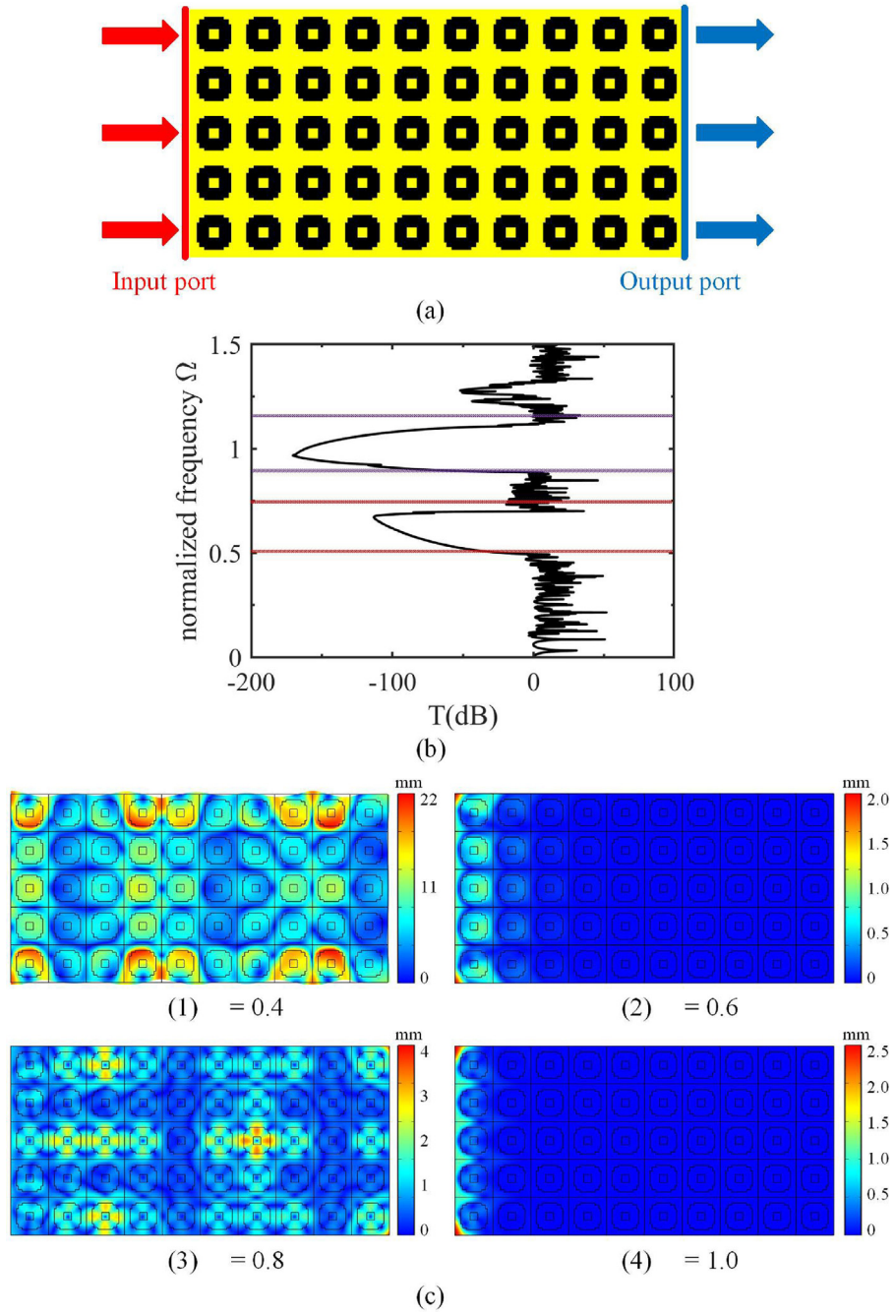

Fig. 10. (a) Schematic diagram of calculating the 5 × 10 PnC microstructure plate model. (b) Transmission spectrum. (c) Elastic wave transmission amplitude field at different normalized frequencies. . (For interpretation of the references to color in this figure legend, the reader is referred to the web version of this article.)

Declaration of competing interest

No potential conflict of interest was reported by the authors.

Data availability

Data will be made available on request

Acknowledgments

The project was supported by the National Natural Science Foundation of China (Grant No. 12072222, 12132010, 12021002, 11991032), the State Key Laboratory of Mechanical Behavior and System Safety of Traffic Engineering Structures, China (Grant No. SKLTESKF1901), and the Aeronautical Science Foundation of China (Grant No. ASFC-201915048001).

References

[1] X.F. Li, X. Ni, L. Feng, M.H. Lu, C. He, Y.F. Chen, Tunable unidirectional sound propagation through a sonic-crystal-based acoustic diode, Phys. Rev. Lett. 106 (2011) 084301.

[2] W. Lee, H. Lee, Y.Y. Kim, Experiments of wave cancellation with elastic phononic crystal, Ultrasonics 72 (2016) 128–133.

[3] J. He, Z. Kang, Achieving directional propagation of elastic waves via topology optimization, Ultrasonics 82 (2018) 1–10.

[4] M.M. Sigalas, C.M. Soukoulis, Elastic-wave propagation through disordered and/or absorptive layered systems, Phys. Rev. B 51 (1995) 2780–2789.

[5] M. Åberg, P. Gudmundson, The usage of standard finite element codes for computation of dispersion relations in materials with periodic microstructure, J. Acoust. Soc. Am. 102 (1997) 2007–2013.
[6] M.M. Sigalas, N. García, Theoretical study of three dimensional elastic band gaps with the finite-difference time-domain method, J. Appl. Phys. 87 (2000) 3122–3125.
[7] M.M. Sigalas, E.N. Economou, Elastic and acoustic wave band structure, J. Sound Vib. 158 (1992) 377–382.
[8] Z. Liu, B. Wu, C. He, Band-gap optimization of two-dimensional phononic crystals based on genetic algorithm and FPWE, Waves Random Complex Media 24 (2014) 286–305.
[9] L. Xie, B. Xia, J. Liu, G. Huang, J. Lei, An improved fast plane wave expansion method for topology optimization of phononic crystals, Int. J. Mech. Sci. 120 (2017) 171–181.
[10] X.K. Han, Z. Zhang, Bandgap design of three-phase phononic crystal by topological optimization, Wave Motion 93 (2020) 102496.
[11] G. Yi, B.D. Youn, A comprehensive survey on topology optimization of phononic crystals, Struct. Multidiscip. Optim. 54 (2016) 1315–1344.
[12] Y.F. Li, X. Huang, F. Meng, S. Zhou, Evolutionary topological design for phononic band gap crystals, Struct. Multidiscip. Optim. 54 (2016) 595–617.
[13] A.K. Sharma, M. Kosta, G. Shmuel, O. Amir, Gradient-based topology optimization of soft dielectrics as tunable phononic crystals, Compos. Struct. 280 (2022) 114846.
[14] G.A. Gazonas, D.S. Weile, R. Wildman, A. Mohan, Genetic algorithm optimization of phononic bandgap structures, Int. J. Solids Struct. 43 (2006) 5851–5866.
[15] O.R. Bilal, M.I. Hussein, Ultrawide phononic band gap for combined in-plane and out-of-plane waves, Phys. Rev. E 84 (2011) 065701.
[16] L. Wang, H.T. Liu, Parameter optimization of bidirectional re-entrant auxetic honeycomb metamaterial based on genetic algorithm, Compos. Struct. 267 (2021) 113915.
[17] H.W. Dong, X.X. Su, Y.S. Wang, C. Zhang, Topological optimization of two-dimensional phononic crystals based on the finite element method and genetic algorithm, Struct. Multidiscip. Optim. 50 (2014) 593–604.
[18] H.W. Dong, Topology optimization of two-dimensional asymmetrical phononic crystals, Phys. Lett. A 378 (2014) 434–441.
[19] M.I. Hussein, K. Hamza, G.M. Hulbert, R.A. Scott, K. Saitou, Multiobjective evolutionary optimization of periodic layered materials for desired wave dispersion characteristics, Struct. Multidiscip. Optim. 31 (2006) 60–75.
[20] H.W. Dong, X.X. Su, Y.S. Wang, Multi-objective optimization of two-dimensional porous phononic crystals, J. Phys. D: Appl. Phys. 47 (2014) 155301.
[21] H.W. Dong, Y.S. Wang, Y.F. Wang, C. Zhang, Reducing symmetry in topology optimization of two-dimensional porous phononic crystals, AIP Adv. 5 (2015) 117149.
[22] S. Hedayatrasa, K. Abhary, M. Uddin, Numerical study and topology optimization of 1D periodic bimaterial phononic crystal plates for bandgaps of low order lamb waves, Ultrasonics 57 (2015) 104–124.
[23] S. Hedayatrasa, K. Abhary, M. Uddin, C.T. Ng, Optimum design of phononic crystal perforated plate structures for widest bandgap of fundamental guided wave modes and maximized in-plane stiffness, J. Mech. Phys. Solids 89 (2016) 31–58.
[24] S. Hedayatrasa, K. Abhary, M.S. Uddin, J.K. Guest, Optimal design of tunable phononic bandgap plates under equibiaxial stretch, Smart Mater. Struct. 25 (2016) 055025.
[25] W. Xu, J. Ning, Z. Lin, W. Qi, H. Liu, W. Wang, Multi-objective topology optimization of two-dimensional multi-phase microstructure phononic crystals, Mater. Today Commun. 22 (2020) 100801.
[26] L. Xie, J. Liu, G. Huang, W. Zhu, B. Xia, A polynomial-based method for topology optimization of phononic crystals with unknown-but-bounded parameters, Internat. J. Numer. Methods Engrg. 114 (2018) 777–800.
[27] K. Deb, A. Pratap, S. Agarwal, T. Meyarivan, A fast and elitist multiobjective genetic algorithm: NSGA-II, IEEE Trans. Evol. Comput. 6 (2002) 182–197.
[28] X.K. Han, Z. Zhang, Topological optimization of phononic crystal thin plate by a genetic algorithm, Sci. Rep. 9 (2019) 1–13.
[29] L. He, H. Guo, Y. Jin, X. Zhuang, T. Rabczuk, Y. Li, Machine-learning-driven on-demand design of phononic beams, Sci. China: Phys. Mech. Astron. 65 (2022) 214612.
[30] S.L. Vatanabe, G.H. Paulino, E.C.N. Silva, Maximizing phononic band gaps in piezocomposite materials by means of topology optimization, J. Acoust. Soc. Am. 136 (2014) 494–501.
[31] Y. Zhang, L. Wang, Q. Ding, H. Han, J. Xu, H. Yan, Y. Sun, Q. Yan, H. Gao, Low-frequency property and vibration reduction design of chiral star-shaped compositive mechanical metamaterials, Mech. Adv. Mater. Struct. 29 (2022) 1–15.